Bimetallic Mesoporous MCM-41 Nanoparticles with Ta/(Ti, V, Co, Nb) with Catalytic and Photocatalytic Properties

Viorica Parvulescu *, Gabriela Petcu, Nicoleta G. Apostol, Irina Atkinson, Simona Petrescu, Adriana Baran, Daniela C. Culita, Ramona Ene, Bogdan Trică, Elena M. Anghel *

Posted Date: 19 September 2024

doi: 10.20944/preprints202409.1452.v1

Keywords: Ta/Me-MCM-41; Me (Nb; Ti; V; Co); bimetallic catalysts; photocatalysts; olefine oxidation; organic pollutants

Article

Bimetallic Mesoporous MCM-41 Nanoparticles with Ta/(Ti, V, Co, Nb) with Catalytic and Photocatalytic Properties

Viorica Parvulescu [1,*], Gabriela Petcu [1], Nicoleta G. Apostol [2], Irina Atkinson [1], Simona Petrescu [1], Adriana Baran [1], Daniela C. Culita [1], Ramona Ene [1], Bogdan Trica [3] and Elena M. Anghel [1,*]

[1] Institute of Physical Chemistry-Ilie Murgulescu of the Romanian Academy, 202 Splaiul Independentei, 060021 Bucharest, Romania; vpirvulescu@icf.ro (V.P.), gpetcu@icf.ro (G.P.), irinaatkinson@yahoo.com (I.A), simon_pet@yahoo.com (S.P.) adibaran@gmail.com (A.B.), dculita@icf.ro (D.C.C), ene.ramona@yahoo.com (R.E), manghel@icf.ro (E.M.A.)

[2] National Institute of Materials Physics, Atomistilor 405A, 077125 Magurele, Romania, nicoleta.apostol@infim.ro (N.G.A.)

[3] National Institute for Research & Development in Chemistry and Petrochemistry-ICECHIM, Bucharest, Romania; trica.bogdan@gmail.com (B.T.)

* Correspondence: vpirvulescu@icf.ro (V.P.); manghel@icf.ro (E.M.A.)

Abstract: The bimetallic (Ta/(Ti, V, Co, Nb) mesoporous MCM-41 nanoparticles were obtained by direct synthesis and hydrothermal treatment. The obtained mesoporous materials were characterized by XRD, XRF, N_2 adsorption/desorption, SEM, TEM, XPS, Raman, UV-Vis, PL spectroscopy. A more significant effect was observed on mesoporous structure, typically for MCM-41, and optic properties if the second metal (Ti, Co) does not belong to the same Vb group with Ta as V, Nb. The obtained new nanoparticles were used as catalysts for oxidation with H_2O_2 of olefinic compounds (1,4 cyclohexadiene, cyclohexene, styrene) and photodegradation of organic pollutants (phenol, methyl orange) from water. The results showed improving of activity and selectivity in oxidation reactions by addition of the second metal to Ta-MCM-41 catalyst. The slow addition of H_2O_2 was also be benefit for the selectivity in epoxide products and stability of the catalysts. The band gap energy values decrease in the presence of the second metal and the band edge diagram evidenced positive potential for all the conduction band of the bimetallic samples except TaTi-MCM-41. The higher photocatalytic degradation was obtained for samples with TaTi and TaV.

Keywords: Ta/Me-MCM-41; Me (Nb; Ti; V; Co); bimetallic catalysts; photocatalysts; olefine oxidation; organic pollutants

1. Introduction

The nanomaterials with ordered mesoporous structure have been widely used in catalytic or photocatalytic oxidation of organic compounds from water. In this group of materials, the modified MCM-41 by the inclusion of metals, either into the framework or well dispersed on the pores surface are the most studied due to their excellent properties, such as uniform pores hexagonally arranged, great specific surface area and volume pores values [1-4]. Narrow-pore size distribution, high surface area and pore volume make MCM-41 promising supports for metal and oxide catalysts. A key role in textural, structural and chemical properties of these materials plays the synthesis method. The most extensively studied method is the direct hydrothermal synthesis, i.e., directly adding metal ion precursor to the synthesis gel prior to hydrothermal treatment. Therefore, many heteroatoms such as Ti, V, Mo, W, Cr, Fe, Mn, Co, Ni, Ru, W, Nb, Ta [5-11] have been incorporated into mesoporous silicas by this method and the obtained materials have been largely used as catalysts [1, 2,6-12], adsorbents [13] or photocatalysts for water decontamination [2,4,5,13-15]. The improved performance is attributed to a small loading of the isolated tetrahedrally coordinated metal oxide centers [16]. Thus, studies revealed for V, Nb and Ta species supported on silica, the predominant presence of isolated MeO_4 species [17-20]. The selectivity in the oxidation reactions was attributed to the presence of Me-

 doi:10.20944/preprints202409.1452.v

O-Si bonds in the catalyst structure. Raman results indicated that the incorporation of Ta atom into the MCM-41 structure forms three types of tantalum oxide species: isolated TaO_4 within MCM-41, isolated surface TaO_4, and bulk Ta_2O_5. These species can be individual or coexist, and its relative intensity is dependent on the Ta concentration [18]. The catalytic properties of the surface TaO_4 species are very different to the bulk Ta_2O_5 with acidic characteristics. Mesostructurated oxides were obtained by associating of tantalum oxide with various other cations as Nb, Ti, Cu, Fe or Ni [16, 19-28]. The modified mesoporous oxides with tantalum [25-28] and especially Ta-MCM-41 catalysts [29,30] proved to be active catalysts. However, tantalum is not among the most frequently used and studied metals supported on the surface of mesoporous materials, although the obtained materials have proven catalytic and photocatalytic activity. Active catalysts were thus obtained in the oxidation of styrene, phenol and sulfides with H_2O_2 [26] or tetrahydroperoxide [28]. The supported tantalum catalysts such as Ta-MCM-41, prepared by grafting of $Ta(OEt)_5$ on MCM-41 [29,30], and Ta_2O_5–SiO_2, obtained by sol-gel method [30] were active and selective in the epoxidation of styrene with tert-butyl hydroperoxide [29] and in selective oxidation of a pyrimidine thioether [30]. Notable is the photocatalytic activity in degradation of dyes of tantalum doped titanium dioxide [27]. Dyes represent an enormous risk for the preservation of ecosystems, and for human health [25,27]. Even in low concentrations (e.g. 1.0 mg/L) they prevent the absorption of light in the aqueous environment and, therefore, decrease the photosynthetic activity and the availability of oxygen for the local species. As well dyes are toxic, mutagenic, carcinogenic and non-biodegradable substances [31].

Although a limited number of studies have studied the effect of Nb or Ti on the catalytic or photocatalytic activity of tantalum immobilized on silica support [20, 29], there are no comparative studies on the effect of a larger number of transition metals on tantalum immobilized on MCM-41. Herein, a series of single and binary metal oxide (Ta and Ti, V, Nb or Co) modified mesoporous MCM-41 photocatalysts were prepared using a well-known direct synthesis with hydrothermal treatment. The effect of second metal on structure, texture, optic properties, active species and photocatalytic properties were evaluated. The obtained new photocatalysts with mesoporous structure were used for degradation of organic pollutants (phenol, dyes) from water.

2. Materials and Methods

2.1. Materials

The materials used for the synthesis of Ta/Nb, Ti, V, Co-MCM-41 mesoporous molecular sieves were: tetraethyl orthosilicate (TEOS) and cetyltrimethylammonium bromide (CTMAB), $TaCl_5$, $NbCl_5$, titanyl acetylacetonate, $Co(NO_3)_2{\cdot}6H_2O$ from Merck (Darmstadt, Germany), $VOSO_4{\cdot}5H_2O$ from Fluka (Buchs, Switzerland), sulfuric acid, 1-propanol ($CH_3CH_2CH_2OH$, ACS reagent, ≥99.5 %), ethanol (CH_3CH_2OH ACS reagent ≥*99.5* %) from Sigma-Aldrich (St. Louis, MO, USA) and sodium hydroxide (NaOH, ≥98 %) from Lach-Ner s.r.o. (Neratovice, Czech Republic). Tantalum and Niobium were stabilized with oxalic acid purchased from Merck (Darmstadt, Germany). The olefinic compounds purchased from Merck (Darmstadt, Germany): 1,4 cyclohexadiene - C_6H_8, 97%, cyclohexene –C_6H_{10}, ≥99.5 %, styrene - C_8H_8, ≥99% were oxidized with hydrogen peroxide - H_2O_2, 30%, Merck (Darmstadt, Germany) using Acetonitrile - CH_3CN, 99.8%, Merck (Darmstadt, Germany) as solvent. For the photocatalytic reactions were used Methyl Orange Dye (85%) and phenol (≥99%) from Merck KGaA, Darmstadt, Germany.

2.2. Photocatalysts Preparation

Ta, Nb, Ti, V and Co species were incorporated into the mesoporous molecular sieves of MCM-41 type by direct synthesis and hydrothermal treatment. The metal source was added in situ to the synthesized gel of silica. The molar ratio of Ta/Me was calculated to be 1. In the first step 0.63 g CTMAB were dispersed in 35 g of deionized water and sulfuric acid at pH=1.5. The solution B (2.8M) was obtained from 7.5 g of TEOS, ethanol-Et and 1-propanol-Pr (Et/Pr molar ratio=6.5). After ten minutes in this solution was added $TaCl_5$, oxalic acid and for each sample the aqueous solution of metal precursor. After 1 hour of mixing solution B was added into mixture A and was stirred for another 1 hour. Finally, the pH was adjusted to 10.5 with a 3N NaOH aqueous solution. The aging of

 doi:10.20944/preprints202409.1452.v

the mixture was carried out for 24 hours at room temperature and for 5 days at 100 °C by hydrothermal treatment. The as-synthesized samples were filtered, washed with deionized water, dried at 100 °C for 6 hours and calcined 6 hours at 550 °C in air flow. The percent of each metal in the obtained samples is listed in Table 1.

Table 1. The percent of metals (Me) in the obtained samples a.

Sample	Sample code	Ta, %	Nb, %	V, %	Ti, %	Co, %	Ta/Me[b]
Ta-MCM-41	**Ta**	5.36	-	-	-	-	-
TaNb-MCM-41	**TaNb**	5.36	3.28	-	-	-	0.829
TaV-MCM-41	**TaV**	5.55	-	1.96	-	-	0.789
TaTi-MCM-41	**TaTi**	5.34	-	-	4.23	-	0.329
TaCo-MCM-41	**TaCo**	3.33	-	-	-	2.44	0.445

[a] % weight from XRF; [b] Ta/Me molar ratio from XRF.

2.3. Materials Characterization

The obtained materials were characterized by XRD, XRF, N_2 adsorption/desorption, SEM and TEM microscopy, Raman, XPS, UV-Vis, PL spectroscopy.

X-ray diffraction (XRD) analysis was performed using a Rigaku Ultima IV diffractometer (Rigaku Corp., Tokyo, Japan) with Cu Kα, λ = 0.15406 nm. Phase evaluation was made with the help of Rigaku PDXL software with Whole Powder Pattern Fitting (WPPF) module, connected to the database ICDD-PDF-2. Using a Rigaku ZSXPrimus II spectrometer (Tokyo, Japan), elemental analysis of the samples was carried out under vacuum. Combining the EZ-scan with the Rigaku SQX fundamental parameters software (Version 5.18) (standard less), which can automatically correct for all matrix effects, including line overlaps, allowed for an analysis of the test results.

Micromeritics ASAP 2020 instrument (Norcross, GA, USA) was utilized to perform N_2 physisorption analysis on the samples for textural characterization. Prior to every measurement, the samples were degassed for five hours at 300 °C under vacuum. The BET model was used to calculate the apparent surface areas from the adsorption branches, while the amount of nitrogen adsorbed at the relative pressure of 0.99 was used to calculate the total pore volume. The t-plot method was used to calculate the micropore and mesopore volumes as well as their surface areas.

The morphology and microstructure of the samples were explored by a scanning electron microscopy (SEM) FEI Quanta 3D FEG and transmission electron microscopy (TECNAI 10 G2-F30 and F20 G2 TWIN Cryo-TEM -FEI).

UV-Raman spectra were collected by means of the a LabRam HR800 spectrometer (HORIBA FRANCE SAS, Palaiseau, France) equipped with a CCD detector and gratings of 2400 gr/mm. A He-Cd laser operating at 325 nm was used as exciting radiations through a 40× NUV microscope objective from Olympus (Olympus Corporation, Tokyo, Japan).

DR-UV/Vis spectroscopy was used to detect the coordination states of 3d metallic species (Co, Nb, V, Ti) added to Ta-MCM-41 by direct synthesis. The spectra of the samples were recorded in the range of 200–850 nm using a JASCO V570 spectrophotometer (Tokyo, Japan). The band gap energies of all the samples were obtained for direct and indirect transitions from the Tauc's plot using the Kubelka–Munk function [32].

For the XPS measurements, the AXIS Ultra DLD installation (Kratos Surface Analysis, Manchester, UK) was used, using an Al Kα1 radiation (1486.74 eV) produced by a monochromatized X-ray source with a power of 144 W (12 kV × 12 mA). The high-resolution spectra were recorded using the "hybrid lens" mode, with a pass energy of 40 eV and a "slot" aperture. The binding energy scale was calibrated to the "standard" C 1s value of 284.6 eV, and the spectra of the levels of interest (Co 2p, O 1s, V 2p, Ti 2p) were analyzed using Voigt profiles, methods described in ref. [33].

The photoluminescence spectra of the samples were obtained using an FLSP 920 spectrofluorimeter (Edinburgh Instruments, Livingston, UK) with a Xe lamp as an excitation source (λ_{exc} = 320 nm). For all measurements, excitation and emission slits were 7 nm.

 doi:10.20944/preprints202409.1452.v

Oxidation of the olefinic compounds with hydrogen peroxide was carried out simultaneously in 5 thermostated microreactors (65 °C), each using 0.05 g of catalyst. Acetonitrile was used as solvent. The molar ratio: organic compound/solvent/hydrogen peroxide was 1/1.8/3. Hydrogen peroxide was added in the first time of reaction or, by dropwise, during the first 3 hours of the reaction (slow addition). The hot filtration experiments were performed by separating the catalyst from the reaction mixture after 5 h of reaction time, and the filtrate was then kept at the reaction temperature for additional 48 h. The reaction products were filtered through Millipore membrane filters and analyzed on a DANI GC 1000 gas chromatograph equipped with a metal capillary column using a flame ionization detector (FID). A hot filtration experiment was performed by separating the catalyst from the reaction mixture after 5 h of reaction time, and the filtrate was then kept at the reaction temperature for additional 48 h. Leaching during the reaction was verified. Thus, the catalyst was recovered from reaction medium, washed with acetonitrile, separated by centrifugation, dried at 80 °C, reactived in air alt 350 °C in order to remove the possible adsorbed compounds [9] and the reused in reaction. The photocatalytic activity of modified Ta-MCM-41 samples was evaluated in oxidative degradation of phenol (Ph) in aqueous solution (0.002 M) and methyl orange dye (MO)- concentration of solution 1·10-5 M. The photocatalytic tests were conducted under stirring in a closed room at 30 ◦C by adding 2 mg of the photocatalyst in 10 mL aqueous solution of reactant. The reaction mixture was stirred in darkness for 30 min to allow the adsorption of organic compounds from solution on the surface of photocatalyst. Further, a UV mercury lamp (60W- with filter of 254 nm was used for irradiation. At certain intervals of time, 2 mL of the mixture was taken out, and the photocatalyst was separated by centrifucation and further using a Millipore syringe filter of 0.45 μm. The filtered solution of dye was spectrophotometrically measured using the same JASCO V570 UV–Vis spectrophotometer. The photocatalytic degradation efficiency was expressed as Ct/C0, where Ct is the concentration of the solution at time t = 1, 3, or 5 h and C0 is the initial absorbance of MO or Ph at t = 0.

3. Results and discussions

3.1. Characterization of materials

In this study, bimetallic MCM-41 ordered mesoporous molecular sieves MCM-41 with Ta/ Nb, Ta/V, Ta/Ti, Ta/Co were successfully prepared. The powder XRD diffractograms of Ta-MCM-41 and Ta/Me-MCM-41 samples obtained at low angle are depicted in Figure 1. It can be seen a distinct and sharp peak (d100) along with weaker and broadening secondary peaks of the (110) and (200). For the samples with second metal near Ta into the MCM-41 structure, the intensity of the first peak decreases and the secondary peak declines or vanishes, indicating structural distortions caused by metal incorporation [34].

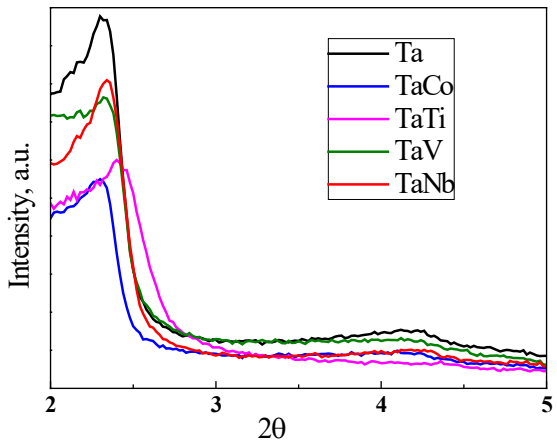

Figure 1. The low-angle XRD patterns of the obtained nanomaterials.

 doi:10.20944/preprints202409.1452.v

The decrease more significant of the first peak intensity and its slight shift is observed for the samples with Ti and Co. Table 1 also show the significant decreasing of the Ta/Me molar ratio for these samples. For the similar synthesis conditions in the case of samples with Nb and V this ratio is closer to 1, the value calculated for these syntheses. Additionally, high angle XRD patterns (Figure S1) showed no characteristic peak regarding to crystalline metals (Nb, V, Ti, Co) species oxides only a broad peak at around $2\theta = 23^{\circ}$ which proof the presence of well dispersed amorphous species and silica support. TEM images of Ta-MCM-41 (Figure 2a) and Ta/Me-MCM-41 (Figure S2) samples indicate the presence of materials with ordered porous structure in a high percent with cylindrical pore channels conformed in a hexagonal array. In Figure 2b, TEM image shows a spherical morphology for the majority of nanoparticles with dimensions close to 100 nm. Many of these nanoparticles are agglomerated to form spherical packages or of wire-like shapes.

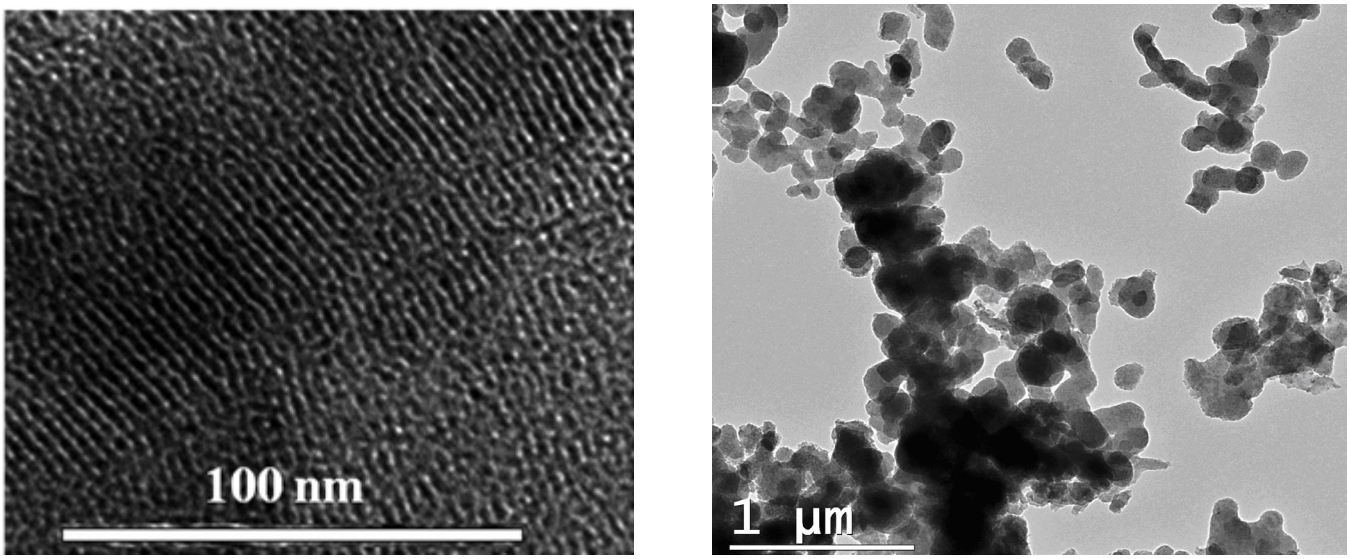

(a) (b)

Figure 2. TEM images of Ta-MCM-41 samples.

SEM microscopy images for the obtained samples, illustrated in Figure 3, confirm the spherical morphology of the agglomerated nanoparticles which may be completed for the bimetallic samples by the wire-like shapes.

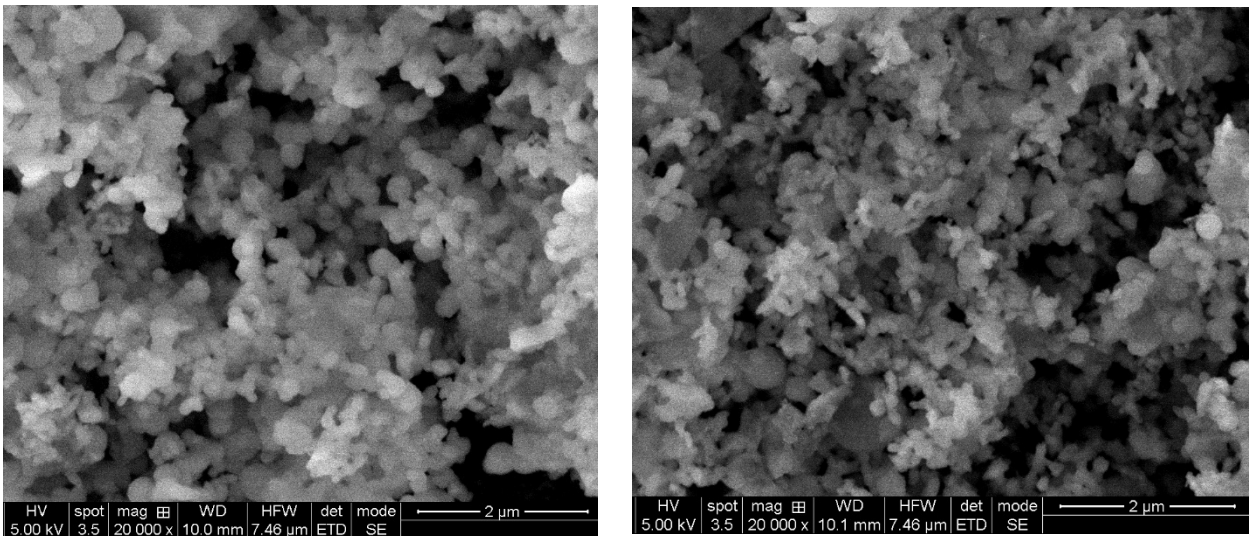

Ta-MCM-41 **TaNb-MCM-41**

 doi:10.20944/preprints202409.1452.v

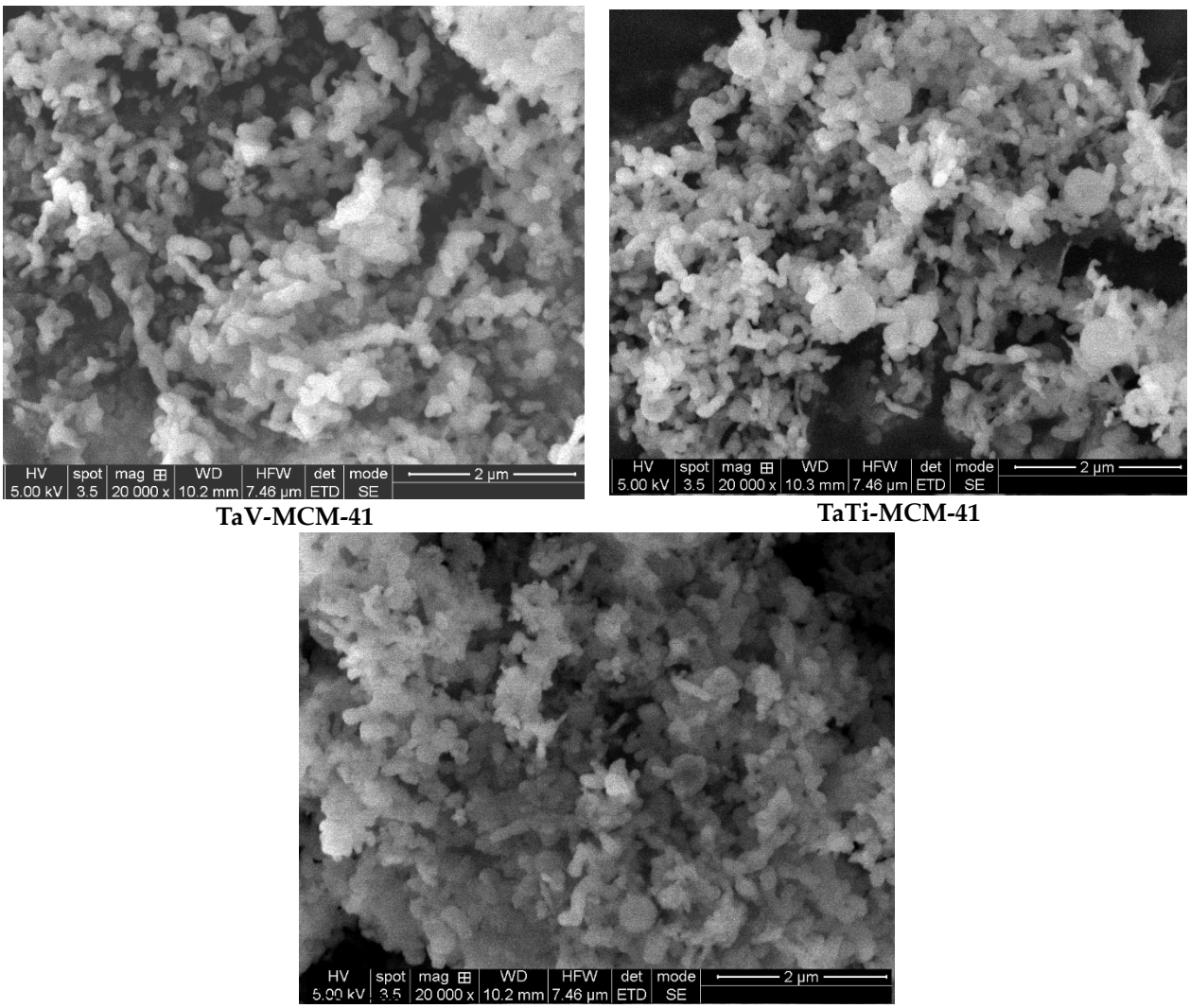

Figure 3. SEM images of the Ta and bimetallic Ta (Nb, V, Ti, Co) samples.

The textural properties of the catalysts have been determined by the N_2 absorption–desorption isotherms of nitrogen. Figure 4 show type IV nitrogen physisorption isotherms which general characteristic for mesoporous materials. The H1 hysteresis loop of isotherms is insignificant which indicates a narrow variation in pore size, except for the TaNb sample. Table 2 presents the variation of the specific surface area, pore volume, and pore sizes of the obtained samples. These samples showed large surface area and pore size diameter similar to those reported for Me-modified MCM-41 mesoporous materials [8,9].

 doi:10.20944/preprints202409.1452.v

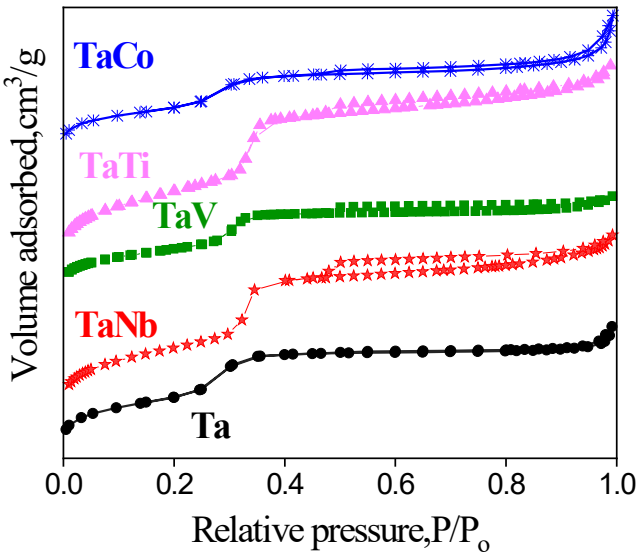

Figure 4. N_2 adsorption-desorption isotherms of Ta/Me-MCM-41 modified samples. .

Table 2. Variation of textural parameters and band gap energy for the obtained samples.

Sample	Ta	TaNb	TaV	TaTi	TaCo
S_{BET} (m^2/g)	867	856	862	826	817
V_{BJH} (cm^3/g)	0.877	0.942	0.894	1.012	1.025
D_{BJH} (nm)	2.9	3.1	2.8	3.0	3.9
Eg (eV)	5.64	3.32	2.18	3.62	2.25

The insignificant changes in the pore diameter can be due to a very good dispersion of the metallic species into the silica mesoporous network and on the pore surface.

The Raman spectra of monometallic(Ta, Nb, V, Ti, Co)-MCM-41 samples (Figures S3 and Table S1 [34-42]) are dominated by the spectra features of the n-membered SiO_4 rings (where n is within 3-7) of the MCM-41 [34,35]. The 490 and 606 cm^{-1} bands belong to the defect bands of the 4- and 3-membered SiO_4 rings. The Raman modes for the 4-membered SiO_4 rings are shifted towards lower wavenumbers at 481 cm^{-1} under the vanadium influence [37]. The distinct band at about 657 cm^{-1} in the Ta-MCM-41 (Ta) spectrum belongs (Figure 5) to the Ta-O-Ta (TaO_6) stretching mode in crystalline Ta_2O_5 [38] which is the major tantalum phase.The 808 cm^{-1} band is due to the symmetric stretching modes of the SiO_4 tetrahedra in the MCM-41 [34].

The total or partial incorporation of metal oxides into the MCM-41 structure is depicted by the bands within the 900-1200 cm^{-1} range in the Si-O stretching domain [34,35].Thus, the weak band of the polymerized TaO_x with TaO_4 coordination [38] on the surface of the MCM-41 was noticeable by fitting the Ta spectrum at about 940 cm^{-1} (see Figure 5).Previous ^{29}Si MAS NMR studies [29] highlighted the incorporation of tantalum into the sol-gel obtained silica framework by $(–O–Si)_3–Ta=O$ bonds due to modification of the Q^4/Q^3 ratio in comparison with the silica counterpart (Q^4 and Q^3 represent the SiO_4 tetrahedra with 0 and 1 Non-Bridging Oxygen atom, NBO). The V-MCM-41 spectra show a strong band at about 980 cm^{-1}, possibly due to the stretching of the SiO-H bonds [42]. Since the SiO-H band within 3740-3750 cm^{-1} (isolated hydroxyl groups on the MCM-41 support [42]) is less intense than those of Me-MCM-41 spectra in Figure S3b, the assignment of the 980 cm^{-1} might consist of stretching vibrations Si-O-Si in SiO_4 tetrahedra [43] with 2 or 1 NBOs, e.g. Q^2 and/ or Q^3 units [44].The intense band at about 1100 cm^{-1} in the Ti-MCM-41 spectrum indicates that the tetrahedrally coordinated titanium ion is in a flexible environment [40] hence titanium incorporation into the MCM-41 structure by Si replacement in its sites. The more flexible environments the more shifted to the lower wavenumbers compared to the 1125 cm^{-1} band position assignable to Si-O-Ti for

 doi:10.20944/preprints202409.1452.v

the TS-1 [40]. Raman spectroscopy is a useful technique for hydrogen bonding interactions between catalysts and water [42]. Also, the presence of the isolated hydroxyl groups on the MCM-41 support is validated by the sharp band at about 3740 cm^{-1} [39]. The hydroxyl groups linked to the metal ions give weaker Raman modes at about 3600 cm^{-1}, namely the left-tailed shoulders of the SiO-H band [42]. The small band at about 3610 cm^{-1} (Figure S3b) signals the presence of the Me-OH [45,46] and free water [42].

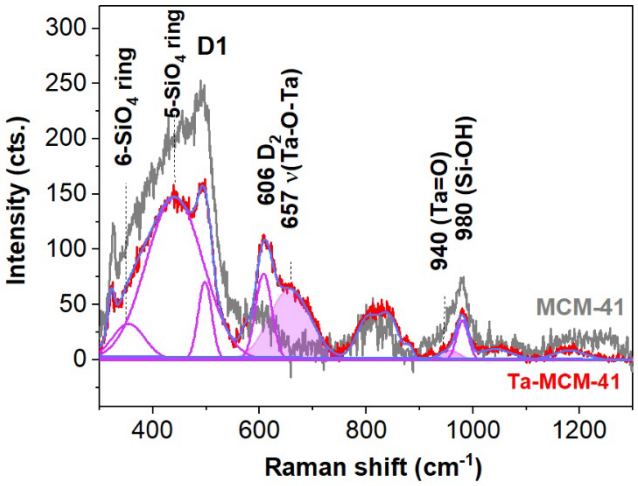

Figure 5. Fitted UV-Raman spectra of Ta-MCM-41 samples (blue line stands for global fit, R^2=0.9902. Some components were left out for clarity). The MCM-41 spectrum was represented for the comparison reason, especially for the wide band at about 800 cm^{-1} which is similar in the two spectra illustrated.

The bimetallic Ta(V,Co,Nb,Ti) samples show spectral features within the 640-745 cm^{-1} range in Figure 6a unlike their (V,Nb,Ti)-MCM41 counterparts (Figure S4, Tables 3 and S1). Fitting of thepeak within 554-758 cm^{-1} for the bimetallic TaTi spectrum revealed three components, namely 607, 616, and 685 cm^{-1}. The 616 cm^{-1} band might be attributable to the A_{1g} modes of the extra-framework TiO_2 as rutile [35]. The most intense band of the Ta-O stretching modes [38] is noticeable at ~ 660 cm^{-1} for the monometallic Ta-MCM-41 spectrum (Table S1).

Table 3. Peak position and assignments for the Ta and bimetallic Ta(Nb, T, Co, V) catalysts within 260-1200 cm^{-1} and 2600-4000 cm^{-1} ranges.

Peak position (cm^{-1})					Assignments	Ref.
Ta	**TaNb**	**TaTi**	**TaCo**	**TaV**	***<650 cm^{-1} n-SiO_4 rings***	34, 35
				355	δ (O-V-O)	36,37
360	348	375	362		5,6,7-SiO_4 rings	34
441	447		435		5,6,7-SiO_4 rings and Eg modes of the extra-framework rutile (445 cm-1)	34, 35
497	496	497	495	488	D_1 modes (4- SiO_4 rings), bending modes of the framework Ti-O-Si speciation	34, 35
608	608	607	612	609	D_2 modes (3- SiO_4 rings)	34
	615	616			υ(Nb-O-Nb) polymerized Nb species (607-650 cm-1) and A_{1g} modes in extra-framework rutile (612 cm^{-1})	48 and 35

 doi:10.20944/preprints202409.1452.v

660		685	670		υ(Ta-O) in TaO6 and Co_3O_4 (690 cm^{-1})	38, 39
	689				Nb_2O_5	48
			707			
	801	798	796		υs modes of the siloxane bridges Si-O-Si	34
828			830		ν_s modes of the siloxane bridges Si-O-Si	34
958		945			υs (Si-O-Ti/Nb)	41
980	978	985	973		υ (Si-OH), ν(Si-NBO) in Q2 units, υ(Nb=O) of isolated NbO_4 and TaO_x species (965-980 cm-1)	34,44, 48 and 18
				1031	$(SiO)_3V=O$ stretching modes	26
				1060	Shorter V=O bonds	47
1050	1056		1065		Q4 units in silica framework	34,44
		1097			υas (Si-O-Ti) with Ti^{4+}	35
1185		1164	1187			
					>3500 cm^{-1} (hydroxyl stretching modes)	
3617		3602	3623	3547	Me-OH and free H_2O	41
3746	3744	3744	3744	3738	Isolated Si-OH in MCM-41	42

νs,as-symmetric, asymmetric stretching, δ-bending vibrations. NBO is non-bridging oxygen. Q2 represents SiO_4 tetrahedra with 2NBO·

Very intense Raman bands of the bimetallic TaV spectrum in Figure 6a are due to anearly resonant effect (UV-VIS absorptions at about 262 and 380 nm of MCM-41 framework and supported vanadium, respectively are presented further in UV-Vis spectra). Atrueresonant effect is expected for the TaCo sample due to its UV absorption at about 320 nm which is very close to the Raman excitation line of 325 nm. The most intense bands of the TaVsample are located at 488 cm^{-1} and 1031 cm^{-1}. At higher vanadium content up to 2wt. %, the tetrahedral vanadate $(SiO)_3V=O$ is responsible for the strong band at ~1031 cm^{-1} [36] while the spectral features of the V_2O_5 (530, 703, and 995 cm^{-1}) are missing from the spectrum. The very weak 920 cm^{-1} of the V-O-V stretching modes indicates that the VO_x clusters are scarce [36,37]. Vibration modes of the tantalum speciation are diminished when compared with 1031 cm^{-1} and 488 cm^{-1}bands (4-membered TO_4 units, where T stands for the tetrahedral coordinated Si or V). The shoulder at about 1060 cm^{-1} might originate from the shorter V=O bonds [47].The tinnySi-OH band at 3738 (Table 3) for the TaVspectrum pointed out that the TaV sample is almost desiccated analogous to the V-MCM-41 sample. This is also supported by the lack of the ~970 cm^{-1} band for Si-OH stretching vibrations in the TaVspectrum. The bimetallicTaNb spectrum has a wide band peaking-up at about 945 cm^{-1} originating from the (Ta,Nb)-O-Si stretching [38]. A less hygroscopic TaNb sample than its Nb-MCM-41 sample is observed in Figure S4.

 doi:10.20944/preprints202409.1452.v

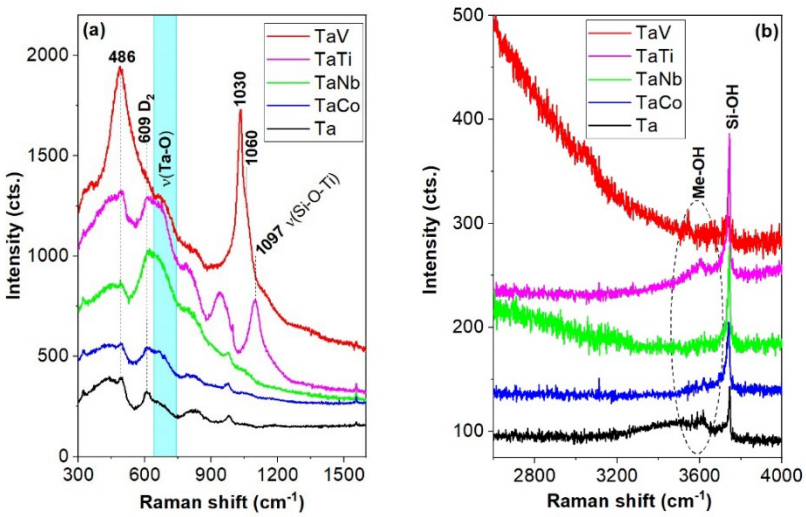

Figure 6. UV-Raman spectra of the Ta, and Ta(Co, Nb, Ti, V) samples.

The pentavalent elements (Ta, Nb and V) were reported to form $(O{=}Me^{5+}\ OSi)_3OH)Si(OH)_2$ and $(O{=}Me^{5+}\ (OSi)_3)Si(OH)$ [49] in hydrated samples. However almost desicated TaV sample were obtained.

XPS was further utilized to analyze the chemical states of elements from the bimetallic materials (TaCo-MCM-41, TaV-MCM-41, TaTi-MCM-41, TaNb-MCM-41) surface. The wide survey spectra Ta/Me-MCM-41 samples showed that all the essential (O 1s, Si 2p, Co 2p, V 2p, Ti 2p, Nb 3d, Ta4f) could be detected (Figure S5). Unfortunately, the intensity of the peak for Nb and Ta are very low. In addition, the peak of Ta4f is masked by that of O2p (Figure 7) in condition of high content of oxygen and lower Ta very dispersed into silica support. The previous studies evidenced changes in coordination for the supported metal oxides of the Group V metals. Thus, the surface tantalum species possess TaO_4 coordination at low surface coverage and highly distorted TaO_5/TaO_6 coordination at intermediate and high surface coverage [50].

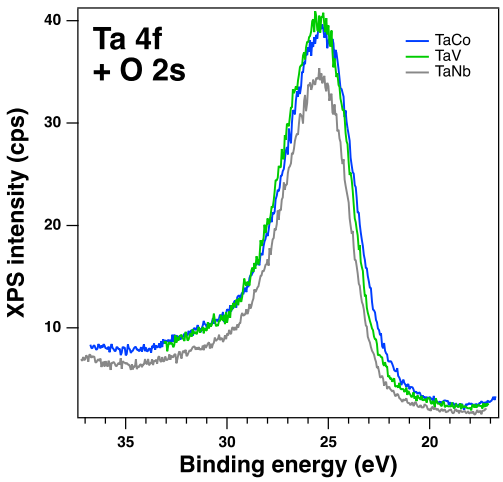

Figure 7. XPS spectra of Ta4f for the bimetallic samples. .

The isolated surface TaO_4 species are present at low surface coverage and especially on the SiO_2 support. Also, on silica surface the maximum achievable density of Ta is much lower than on other oxide supports (~1 toward 5–6 Ta atom/nm^2). Thus, the molecular structures and densities of tantalum and niobium species on surface are very similar. For niobia supported on silica the density is less than 2 Nb atoms/nm^2 [50]. These results can explain the very low intensity of XPS spectra for Ta and Nb. Figures 7, S6 and 8 show significant differences between peaks intensity of the metals immobilized on silica under the conditions of similar Ta/Me molar ratio. These indicated the presence

 doi:10.20944/preprints202409.1452.v

of isolated TaO_4 and NbO_4 species and Ta=O, Nb=O bonds in strong interaction with silica (Table 3, Figure 6). The spectra of metals associated with Ta are illustrated in Figure 8, except Nb whose XPS spectrum (Figure S6).

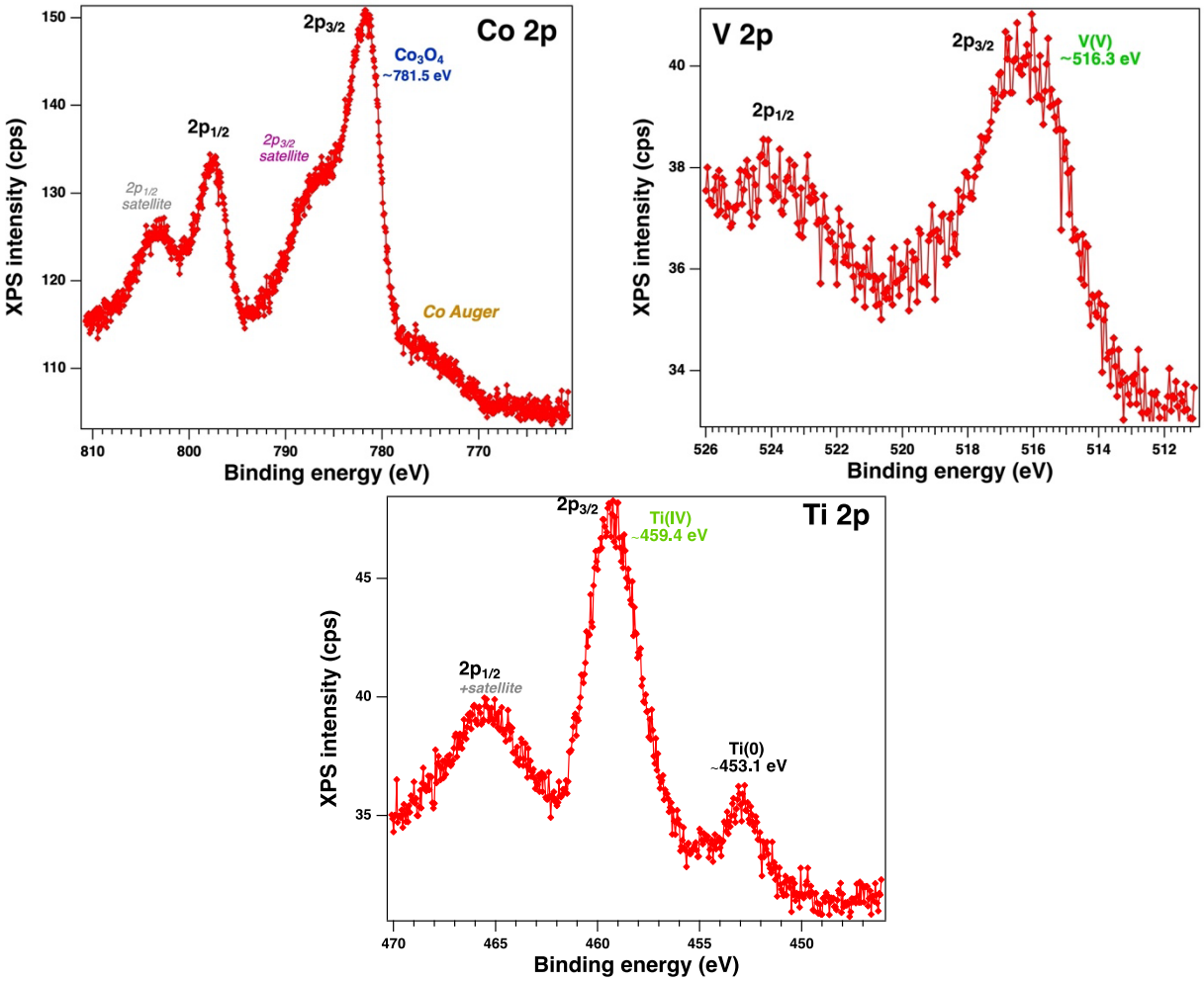

Figure 8. XPS spectra of Co2p, V2p and Ti2p for the samples TaCo-MCM-41, TaV-MCM-41 and TaTi-MCM-41 samples.

The use of Density Functional Theory (DFT) to investigate Ta oxides in various oxidation states was evidenced that stoichiometry and amorphous state change the Coulomb repulsion and hence the binding energies [51]. The results showed a significant fraction of Ta atoms in all samples are under-coordinated state and the longer Ta–O distances in amorphous TaO_x leads to lower Coulomb repulsion and hence higher binding energies. These results can explain difficulty in analysis of XPS spectra both for Ta and the other oxide species incorporated into MCM-41 mesoporous silica by direct synthesis in lower quantity [52,53].

The analyzed spectra of Co 2p, V2p and Ti2p revealed the coexistence of different chemical states of each metal. Co 2p spectrum presents two main components and their satellites, at binding energies (BE) of 782.9 eV and 781.2 eV, attributed to 2+ and 3+ chemical states of cobalt from Co_3O_4. The spectrum of V 2p shows a main peak at around 516 eV and the presence of the satellite at ~523 eV attributed to V_2O_5. These results agree with others published results [54] that evidenced two main different coordinated forms for the isolated vanadium species on support: tetrahedral V^{5+} of type (VO_4^{3-}) and tetrahedrally coordinated vanadium sites ($(SiO)_3V=O$). XPS narrow scan of Ti 2p indicate that the valence state of Ti from TaTi-MCM-41 sample is Ti^{4+} and Ta^{0+} [55-57]. Spectra of Nb3d from TaNb-MCM-41 sample (Figure S6) can be attributed to Nb_2O_5 high dispersed into MCM-41 network. These results confirm the interaction of metals and their specific distribution on mesoporous silica support. The high-resolution spectra of O1s evidence (Figure S7) the presence of main two kinds of

 doi:10.20944/preprints202409.1452.v

chemical environments: lattice oxygen from silica with shifted binding energy at around 532 eV and oxygen vacancies or oxygen deficient regions from surface (~ 533 eV). XPS spectra of O1s show, for TaTi-MCM-41 sample, a peak at around 524 eV which indicates the presence on the surface of Me-O bonds that the more ionic than the Si-O bond [58].

UV–Vis diffuse reflectance spectra of the synthesized samples are shown in Figure 9. For all the samples it was noticed an absorption band at around 263 nm, associated with the charge transfer from oxygen ions of MCM-41 framework to the metal in tetrahedral coordination [13].

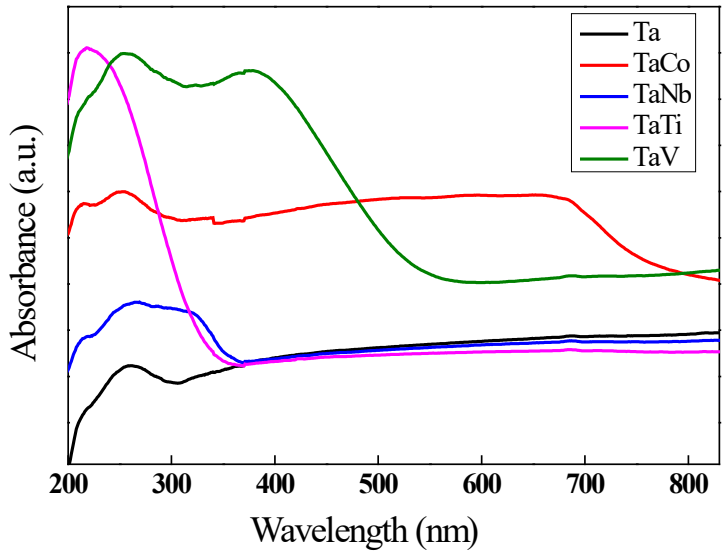

Figure 9. Diffuse reflectance UV–vis spectra of Ta-MCM-41 sample and Ta-MCM-41 modified with Co, Nb, Ti, V by direct synthesis.

Two other intense absorption bands were observed for TaNbMCM-41 and TaVMCM-41, located at around 318 nm and 380 nm, respectively. Their presence indicates the formation of crystalline Nb_2O_5 [19], and V_2O_5 [59] in the modified materials. TaVMCM-41 sample exhibited a very broad band between 250 and 550 nm, due to the charge transfer associated with V-O electron transfer for tetrahedrally coordinated V^{5+} species. In the case of Ti modification, an intense band at 220 nm appears (TaTiMCM-41 sample). It corresponds to ligand-to-metal charge transfer (LMCT) from oxygen to tetracoordinated titanium in isolated tetrapodal ($Ti(OSi)_4$) or tripodal (such as, $Ti(OH)(OSi)_3$) units. The presence of this absorption band suggests the successful incorporation of Ti as isolated species into the silica structure. Furthermore, the shoulder located at higher wavelength (~270 nm) indicates the presence of higher coordinated Ti species (penta- or hexacoordinated) which could occur through hydration by binding water molecules as extra ligands [60].

Modification of Ta-MCM-41 with the transition metals Co, Nb, V, and Ti by direct synthesis led to a redshift of absorption spectra in all cases. Thus, the synthesized materials became active under visible light irradiation by lowering the energy of the band gap considerably compared to the sample Ta-MCM-41, as shown in Table 2.

The photoluminescence (PL) spectra (Figure 10) were determined to evaluate the separation and recombination of the photogenerated charges in Ta-MCM-41 and Ta/Me-MCM-41 samples. The PL intensity is influenced by both surface defects and internal defects. All the spectra exhibit two emission peaks at around 425 nm and 490 nm. The highest intensity of both peaks was obtained for TaTi-MCM-41 spectra. The PL spectrum of this sample indicates a stronger activation but also a lower stability. The first peak was attributed to the band-to-band direct transitions. The intensity of this peak decreases in the following order Ta>TaNb>TaV>TaCo due to the higher electron-hole separation that gives long-lived photogenerated charge carriers [61,62].

 doi:10.20944/preprints202409.1452.v

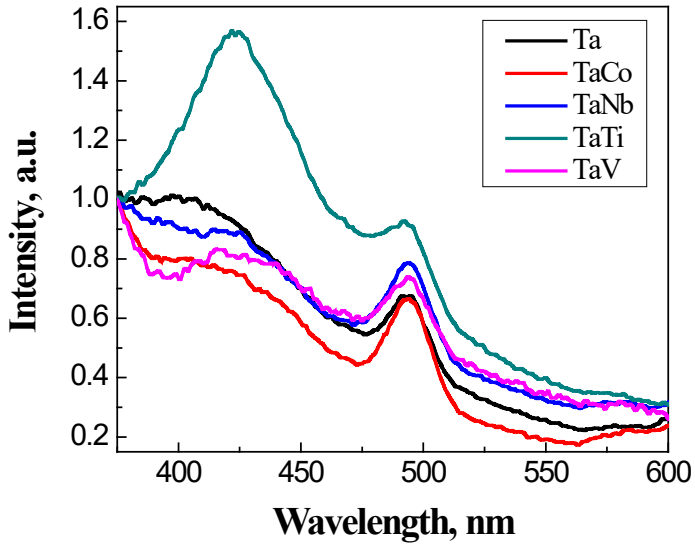

Figure 10. PL spectra of the obtained samples.

At the same time, a shift to 400 nm can be observed and for the bimetallic samples. The second excitonic PL peak (490 nm) suggests that the samples contain high defects generated by metals incorporation. Surface defects refer primarily to the presence of metal ions dispersed on the silica surface and the incomplete coordination of surface species that induce oxygen vacancies. Thus, recombination centers for charge carriers are created. Also, the high dispersion of metal ions and the possibility of incorporating them into the silica network generate defects that act as donors or acceptors [23,63].

3.2. Catalytic Properties

All the obtained materials are active and selective in oxidation of the olefinic double bands with H_2O_2. The oxidation of organic molecules under mild conditions is a topic of great interest [25,27-29,64]. A higher conversion was obtained in oxidation of 1, 4 cyclohexadiene on TaCo and Ta Nb catalysts (Figure 11). The increasing of conversion was also evidenced for TaTi sample.

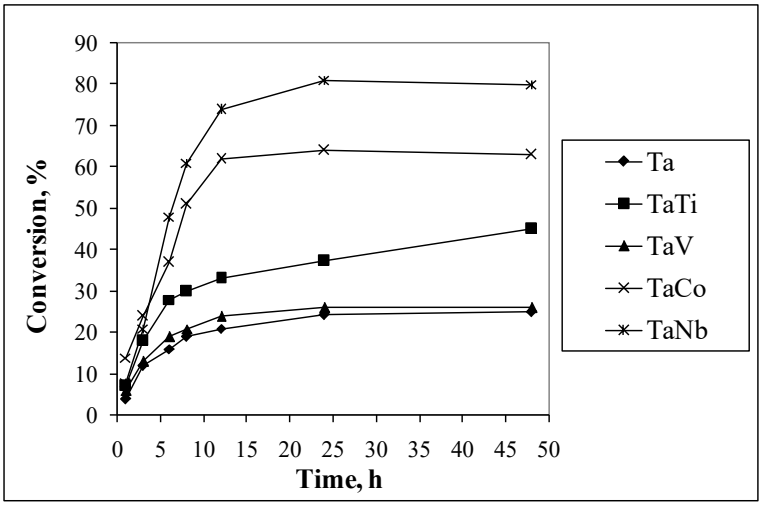

Figure 11. Conversion of 1,4 cyclohexadiene as a function of time reaction (slow addition of H_2O_2).

The activity and selectivity to epoxide of the Ta mesoporous molecular sieves (Table 4) was influenced by the composition of the catalyst and kinds of H_2O_2 addition. The effect of slow addition of H_2O_2 was evidenced in Figure 12. It can see that the conversion of the samples marked with s (slow

 doi:10.20944/preprints202409.1452.v

addition of H_2O_2 during the first 3 hours of the reaction) is higher compared with the reactions in which the entire amount of hydrogen peroxide was added at the beginning of the reaction. These results indicate that the adsorption is a limitative step of the oxidation reaction.

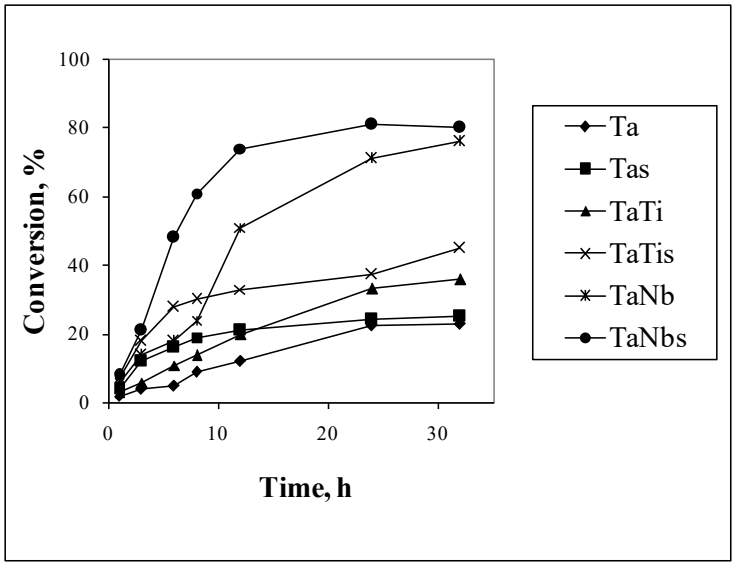

Figure 12. Effect of H_2O_2 addition on conversion of **1,4 cyclohexadiene.**

The main reaction products were: cyclohexenone and cyclohexenol for oxidation of 1, 4 cyclohexadiene; cyclohexene oxide, cyclohexenone, cyclohexenol for oxidation of cyclohexene; benzaldehyde and styrene oxide in case of styrene oxidation. The second metal and slow addition of H_2O_2 favor the selectivity to epoxide. The selectivity to epoxide (cyclohexene oxide –HO and styrene oxide -SO) was high in oxidation of cyclohexene and styrene for all the bimetallic catalysts. Higher selectivity to cyclohexenol was obtained for all the catalysts (Table 4).

Table 4. Results of the catalytic tests. .

Sample	1,4 Cyclohexadiene		Cyclohexene		Styrene	
	C (%)	S_{HOL} (%)	C (%)	S_{HO} (%)	C (%)	S_{SO} (%)
Ta	25.2	91.2	28.1	25.2	48.1	21.2
Ta Nb	81.1	85.2	65.7	71.2	76.4	65.0
TaV	36.1	84.5	32.4	78.9	89.0	66.8
TaTi	37.4	98.6	56,3	89.4	95.0	62.6
TaCo	64.0	89.0	64.2	84.4	78.2	71.2

3.3. Photocatalytic Properties

Ta-based photocatalysts has also garnered considerable attention in photocatalytic applications due to their electronic structure and high chemical stability [13,16,23,65,66]. Thus, the photocatalytic properties of tantalum-based mesoporous materials were tested in the oxidative degradation reaction of phenol (Ph) and methyl orange (MO). These organic compounds are the main representative for the common pollutant from waste water, as phenol and dyes, for which it is of particular interest [67-69]. For a better understanding of the effect of Ta-MCM-41 modification with different 3d metals (Co, Nb, V) on photocatalytic properties, the valence band (VB) energy of each sample was estimated from the valence band (VB) XPS measurements (Figure S8). The results revealed the VB maxima of 4.5 eV for the TaNbMCM-41 sample, very close to the VB potential of TaVMCM-41 (4.3 eV), 3.6 eV for TaCoMCM-41, and 2.8 for TaTiMCM-41. The conduction band (CB) potential of the synthesized materials was obtained using the following Equation (1):

$$E_{CB} \text{ (vs. NHE)} = E_{VB} \text{ (vs. NHE)} - E_g \quad (1)$$

where E_{CB} is CB potential, E_{VB} is VB potential, and E_g is band gap energy [70,71].

 doi:10.20944/preprints202409.1452.v

Based on the obtained values of the valence, conduction bands, band gape energy and redox potentials for generation of $\bullet O_2^-$ and •OH oxidative radicals are presented in Figure 13. It can observe that the CB energy level is higher than the normal redox potentials of $O_2/\bullet O_2^-$ for all the bimetallic samples except TaTi.

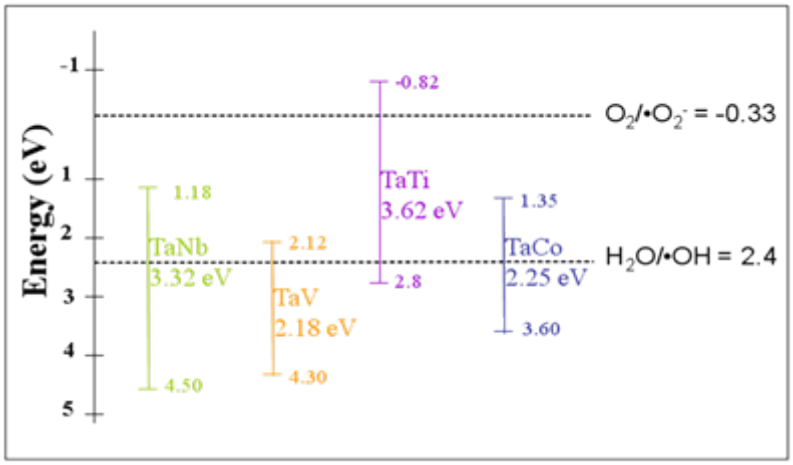

Figure 13. Energy band diagram for the bimetallic Ta/Me samples.

At the same time, VB energy level is more positive for all the samples than the $H_2O/\bullet OH$ potential (+2.40 eV) which leads to the generation of the •OH radicals [66]. Therefore, only for TaTi sample photogenerated e^- has been able to reduce O_2 to $\bullet O_2^-$. Hence, it means that only TaTi-MCM-41 sample is favorable for both oxidation and reduction reactions. These results were confirmed by the photocatalytic tests carried out for the degradation of methyl orange in aqueous solution. Figure S9 shows a significant absorption of MO on the photocatalyst surface. However, under irradiation, the MO concentration decreases only in the case of the TaTi sample. In presence of H_2O_2 de efficiency of MO degradation increased significant for all the photocatalysts Figure 14. A similar stability was evidenced for Fe_3O_4@SiO_2@ZnO composite in photodegradation of MO under UV [72]. The significant increase in the MO photodegradation efficiency was achieved by adding H_2O_2. As an electron acceptor, H_2O_2 generated hydroxyl radicals ($H_2O_2+e^- \rightarrow OH^- + \bullet OH$). Thus, the possibility of photogenerated e^-/h^+ recombination was reduced and the number of •OH radicals on the surface increased. Since in the case of the synthesized materials, excepting TaTi sample, the photogenerated electrons can not form $\bullet O_2^-$ radicals with O_2, they can inhibit the photocatalytic reaction by recombining with the holes. For this reason, the photocatalytic reactions have been performed in the presence of H_2O_2.

In degradation of phenol the higher efficiency was obtained for TaTi and TaV samples (Figure 14).

 doi:10.20944/preprints202409.1452.v

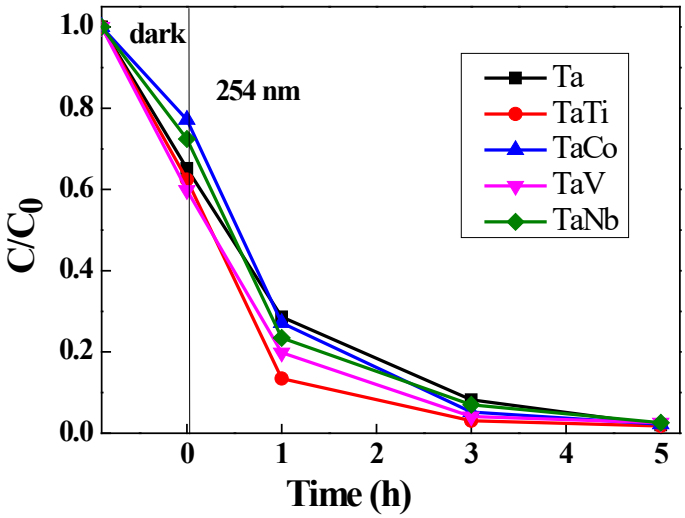

Figure 14. Photodegradation of methyl orange with H_2O_2 under UV light.

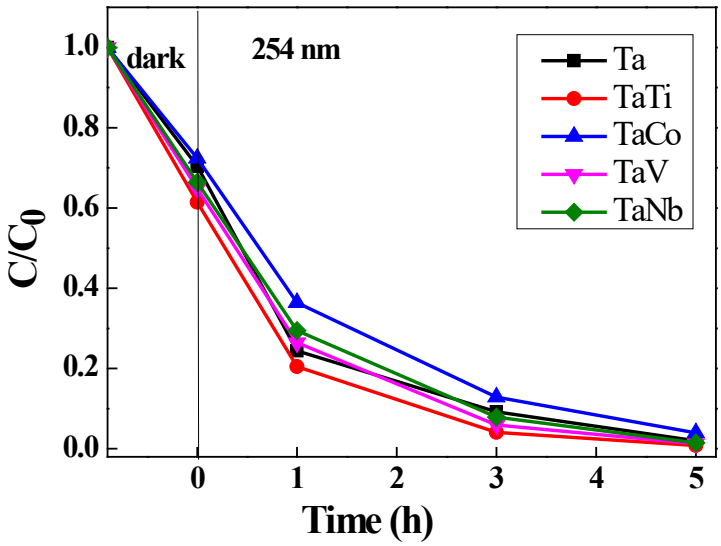

Figure 15. Oxidative photodegradation of phenol under UV light in presence of H_2O_2.

The mechanism proposed for these oxidation reactions with hydrogen peroxide marked formation of •OH with $•O_2^-$ species [68]. The obtained results recommend the modified Ta-MCM-41 materials as catalysts for oxidation of organic compounds and confirm their possible application in photocatalytic reactions. Furthermore, the maximum degradation of MO and Ph was obtained for all the samples in the presence of H_2O_2. The degradation of these organic pollutants, at macro level, is most probably due to the synergistic effect of adsorption and photocatalytic oxidation, whereas at the micro level, the degradation is the result of a large number of hydroxyl radicals resulted in the presence of H_2O_2 and photocatalytic process.

4. Conclusions

New bimetallic Ta(Ti, V, Co, Nb) mesoporous nanomaterials were obtained by direct synthesis method. The effect on the mesoporous structure, typically for MCM-41, and optic properties of second metal (Ti, Co) is more pronounced. Ta_2O_5 presence and partially (V, Nb) or complete (Ti) incorporation as $(SiO)_3Me{=}O$ into MCM-41 framework was depicted by Raman findings. The expectation from this behavior is represented by cobalt. Despite the resonant effect (namely UV-adsorption at the same wavelength as the Raman excitation), only Co_3O_4 was observed by Raman spectra deconvolution. All the catalysts were active in oxidation with H_2O_2 of olefinic compounds

 doi:10.20944/preprints202409.1452.v

(1,4 cyclohexadiene, cyclohexene, styrene). The second metal and slow addition of H_2O_2 favor the selectivity to epoxide. The selectivity to epoxide was high in oxidation of 1, 4 cyclohadiene and cyclohexene for all the bimetallic catalysts. The insignificant methyl orange photodegradation on all the catalysts, except TaTi-MCM-41, was explained by positive conduction band (CB) potential, higher than the normal redox potentials of $O_2/\bullet O_2^-$. In presence of H_2O_2 methyl orange and phenol were total photodegradated. As an electron acceptor, H_2O_2 captured photogenerated electrons, blocking their recombination with holes, and generated more hydroxyl radicals increasing the photocatalytic activity.

Supplementary Materials: Figure S1: The high angles XRD diffractograms of TaMe/MCM-41 samples; Figure S2: TEM images of Ta-MCM-41 (a); TaV-MCM-41 (b); TaTi-MCM-41 (c); TaNb-MCM-41 and TaCo-MCM-41 samples; Figure S3: Raman spectra of the monometallic (Ta,V, Ti,Nb,Co)-MCM-41; Figure S4: Comparative Raman spectra of monometallic (Ta, V,Ti,Nb,Co)-MCM-41 and bimetallic Ta(V, Ti,Nb,Co) samples; Figure S5: XPS full scan survey spectra for the bimetallic Ta/Me samples; Figure S6: XPS spectra for Nb3d of TaNb-MCM-41 sample**;** Figure S7: XPS spectra for O1s of the bimetallic Ta/Me-MCM-41 samples**;** Figure S8: XPS valence band spectra of the bimetallic Ta/Me samples; Figure S9: Photodegradation of methyl orange in aqueous solution; Table S1: Peak position and assignments for the monometallic (Ta/Nb/Ti/Co/V)-MCM41 catalysts.

Author Contributions: Author Contributions: Conceptualization, V.P.; methodology, V.P.; validation, V.P.; formal analysis, E.M.A.; investigation, V.P., E.M.A., G.P., N.G.A., I.A., S.P., A.B., D.C.C., R.E. and B.T.; data curation, E.M.A., G.P., N.G.A., I.A., S.P., A.B., D.C.C., R.E. and B.T.; writing—original draft preparation, V.P., E.M.A. and G.P.; writing—review and editing, V.P. and E.M.A.; visualization, V.P.; supervision, V.P. All authors have read and agreed to the published version of the manuscript.

Data Availability Statement: The data presented in this study are available on request from the corresponding author.

Acknowledgments: This research was funded by the Ministry of Research, Innovation and Digitization, through the PN 23.06 Core Program—ChemNewDeal within the National Plan for Research, Development and Innovation 2022–2027, project No. PN 23.06.02.01 (InteGral).

Conflicts of Interest: The authors declare no conflict of interest.

References

1. Morais, L.A.; Castro, F. L.; Fernandes, G.J.T.; Araujo, M.D.S.; Farias, M.F.; Guedes, A.P.M.A.; Fernandes Jr., V.J.; Araujo, A.S. Synthesis and Characterization of MCM-41 Nanomaterials Containing Titanium and Application for Catalytic Oxidation of BTEX. *Catalysis Research* **2023**, 3, 17. Doi: 10.21926/cr.2302017
2. Hachemaoui, M.; Molina, C.B.; Belver, C.; Bedia, J.; Mokhtar, A.; Hamacha, R.; Boukoussa, B. Metal-Loaded Mesoporous MCM-41 for the Catalytic Wet Peroxide Oxidation (CWPO) of Acetaminophen. *Catalysts* **2021**, 11, 219. Doi: 10.3390/catal11020219
3. Peng, W.; Cai, L.; Lu, Y.; Zhang, Y. Preparation of Mn-Co-MCM-41 Molecular Sieve with Thermosensitive Template and Its Degradation Performance for Rhodamine B. *Catalysts* **2023**, 13, 991. Doi: 10.3390/catal13060991
4. Sahoo, D.P.; Rath, D.; Nanda, *B.;* Parida, K.M. Transition metal/metal oxide modified MCM-41 for pollutant degradation and hydrogen energy production: a review. *RSC Adv.* **2015**, 5, 83707-83724. Doi: 10.1039/C5RA14555D
5. Schlichter, S.; Sapag, K.; Dennehy, M.; Alvarez, M. Metal-based mesoporous materials and their application as catalysts for the degradation of methyl orange azo dye. *J. Environ. Chem. Eng.* **2017**, 5, 5207-5214. Doi: 10.1016/j.jece.2017.09.039
6. Todorova, S.; Parvulescu, V.; Kadinov, G.; Tenchev, K.; Somacescu, S.; Su, B.-L. Metal states in cobalt- and cobalt-vanadium-modified MCM-41 mesoporous silica catalysts and their activity in selective hydrocarbons oxidation. *Micropor. Mesopor. Mat.* **2008**, 113, 22–30. Doi: 10.1016/j.micromeso.2007.10.047
7. Kilos, B.; M. Nowak, A.I.; Ziolek M.; J.C. Volta, J.C. The role of niobium in the gas- and liquid-phase oxidation on metallosilicate MCM-41-type materials. *J. Catal.* **2004**, 224, 314-325. Doi: 10.1016/j.jcat.2004.03.002
8. Parvulescu, V.; Tablet, C.; Anastasescu, C.; Su, B.L. Activity and stability of bimetallic Co (V, Nb, La)-modified MCM-41 catalysts. *Catal. Today* **2004**, 93-95, 307-313. Doi: 10.1016/j.cattod.2004.06.006

9. Parvulescu, V.; Anastasescu, C.; Su, B.L. Vanadium incorporated mesoporous silicates as catalysts for oxidation of alcohols and aromatics. *J. Mol. Catal. A: Chem.* **2003**, 198, 249-261. Doi: 10.1016/S1381-1169(02)00694-5
10. Genel, S.; Durak, H.; Genel Y.; Catalytic effect of metal powder and MCM-41/metal catalysts on the pyrolysis of cellulose**.** *Environ. Prog. Sustain.* **2024**, 43, 14225**.** Doi: 10.1002/ep.14225
11. Parvulescu, V.; Anastasescu, C.; Su, B. L. Bimetallic Ru-(Cr, Ni, or Cu) and La-(Co or Mn) incorporated MCM-41 molecular sieves as catalysts for oxidation of aromatic hydrocarbons. *J. Mol. Catal. A: Chem*. **2004**, 211, 143-148. Doi: 10.1016/j.molcata.2003.10.011
12. Parvulecu, V. 2-Catalytic behavior of metal active sites from modified silicas in oxidation of organic compounds. In Redox, **2019,** editor Khattak R., IntechOpen, pp 1-25. Doi:10.5772/intechopen.90209
13. Fernandes de Oliveira, T.; Pereira de Souza, C.; Lopes-Moriyama, A. L.; Pereira da Silva M. L. *In situ* modification of MCM-41 using niobium and tantalum mixed oxide from columbite processing for methylene blue adsorption: Characterization, kinetic, isotherm, thermodynamic and mechanism study. *Mater. Chem. Phys.* **2023**, 294, 127011. Doi: 10.1016/j.matchemphys.2022.127011
14. Dubiel, W.; Kowalczyk, A.; Jankowska, A.; Michalik, M.; Mozgawa, W.; Kobielusz, M.; Macyk, W.; Chmielarz, L. Silica-titania mesoporous silicas of MCM-41 type as effective catalysts and photocatalysts for selective oxidation of diphenyl sulfide by H_2O_2. *Green Process. Synth.* **2023**, *12*, 20230052. Doi: 10.1515/gps-2023-0052
15. Arellano, U.; Wang, J.A.; Chen, L.F.; Asomoza, M.; Guzmán, A.; Solís, S.; Estrella, A.; Cipagauta, S.; Noreña, L.E. Transition metal oxides dispersed on Ti-MCM-41 hybrid core-shell catalysts for the photocatalytic degradation of Congo red colorant. *Catal. Today* **2020**, *349*, 128-140. Doi: 10.1016/j.cattod.2018.05.017
16. Nguyen, V.H.; Lin, S.D.; Wu, J. C.-S. Synergetic photo-epoxidation of propylene over V-Ti/MCM-41 mesoporous photocatalysts. *J. Catal.* **2015**, *331*, 217–227. Doi: 10.1016/j.jcat.2015.09.001
17. Brutchey, R. L.; Lugmair, C.G.; Schebaum, L.O.; Tilley, T.D. Thermolytic conversion of a bis(alkoxy)tris(siloxy)tantalum(V) single-source molecular precursor to catalytic tantala–silica materials. *J. Catal*. **2005**, 229, 72–81. Doi: 10.1016/j.jcat.2004.10.015
18. Jehng, J.M.; Tung, W.C.; Huang, C.H.; Wachs, I.E. Structural characteristics and reactivity properties of the tantalum modified mesoporous silicalite (MCM-41) catalysts. *Microporous Mesoporous Mat.* **2007**, 99, 299–307. Doi: 10.1016/j.micromeso.2006.09.036
19. Oliveira, T.F.; Pereira da Silva, M.L.; Lopes-Moriyama, A.L.; Pereira de Souza, C. Facile preparation of ordered mesoporous Nb, Ta-MCM-41 by hydrothermal direct synthesis using columbite ore as metal source. *Ceram. Int*. **2021**, 47, 29509–29514. Doi: 10.1016/j.ceramint.2021.07.120
20. Lee, B.; Yamashita, T.; Lu, D.; Kondo, J.N.; Domen, K. Single-Crystal Particles of Mesoporous Niobium-Tantalum Mixed Oxide. *Chem. Mater*. **2002**, *14*, 867-875. Doi: 10.1021/cm010775m
21. Ziolek, M.; Nowak, I.; Characterization techniques employed in the study of niobium and tantalum-containing materials. *Catal. Today* **2003**, 78, 543-553. Doi: 10.1016/S0920-5861(02)00353-X
22. Takahara, Y.; Kondo, J.N.; Lu, D.; Domen, K. Synthesis and application for overall water splitting of transition metal-mixed mesoporous Ta oxide. *Solid State Ion.* **2002**, *151*, 305-311. Doi: 10.1016/S0167-2738(02)00728-2
23. Yang, X.; Roy, A.; Alhabradi, M.; Alruwaili, M.; Chang, H.; Tahir, A.A. Fabrication and Characterization of Tantalum–Iron Composites for Photocatalytic Hydrogen Evolution. *Nanomaterials* **2023**, *13*, 2464. Doi: 10.3390/nano13172464
24. Oliveira, T.F.; de Souza, C.P.; Lopes-Moriyama, A.L.; Acid leaching and thermal treatments in the obtaining of mixed oxides of Nb and Ta from ferrocolumbite. *Miner. Eng.* **2020,** 147,106157. Doi: 10.1016/j.mineng.2019.106157.
25. Talukdar, H.; Saikia, G.; Das, A.; Sultana, S.Y.; Islam, N.S. Organic-solvent-free oxidation of styrene, phenol and sulfides with H_2O_2 over eco-friendly niobium and tantalum based heterogeneous catalysts. *J. Ind. Eng. Chem*. **2023**, *121*, 249–263. Doi: 10.1016/j.jiec.2023.01.029
26. Paul, R.; Kavinarmatha, K.; Parthiban S. Tantalum doped titanium dioxide nanoparticles for efficient photocatalytic degradation of dyes. *J. Mol. Struct.* **2023**, *1277*, 134869. Doi: 10.1016/j.molstruc.2022.134869
27. Fadhlia, M.; Khedhera, I.; José M. Fraile J.M. Modified Ta/MCM-41 catalysts for enantioselective oxidation of thioanisole. *J. Mol. Catal. A: Chem.* **2015**, *410*, 140–148. Doi: 10.1016/j.molcata.2015.09.017
28. Fadhli, M.; Khedher, I.; Fraile, J.M. Comparison of Ta-MCM-41 and Ti-MCM-41 as catalysts for the enantioselective epoxidation of styrene with TBHP. *C R Chim*. **2017**, *20*, 827-832. Doi: 10.1016/j.crci.2017.02.008
29. Cimpeanu, V.; Pârvulescu, V.; Pârvulescu, V.I.; Capron, M.; Grange, P.; Thompson, J.M.; Hardacre, C. Selective oxidation of a pyrimidine thioether using supported tantalum catalysts. *J. Catal*. **2005**, *235*, 184-194. Doi: 10.1016/j.jcat.2005.08.004

30. Shindhal, T.; Rakholiya, P.; Varjani, S.; Pandey, A.; Ngo, H.H.; Guo, W.; Ng, H.Y. Taherzadeh, M.J. A critical review on advances in the practices and perspectives for the treatment of dye industry wastewater. *Bioengineered* **2021**, 12, 70–87. Doi: 10.1080/21655979.2020.1863034
31. Makuła, P.; Pacia, M.; Macyk,W. How to correctly determine the band gap energy of modified semiconductor photocatalysts based on UV−Vis spectra. *J. Phys. Chem. Lett*. **2018**, 9, 6814–6817. Doi: 10.1021/acs.jpclett.8b02892
32. Teodorescu, C.M.; Esteva, J.M.; Karnatak, R.C.; El Afif, A. An approximation of the Voigt I profile for the fitting of experimental X-ray absorption data. *Nucl. Instrum. Meth. Phys. Res. A* **1994**, *345*, 141–147. Doi: 10.1016/0168-9002(94)90983-0
33. Al Ebraheem, J.S.; Alkhoder, M.N.A.; Tulaimat, R.H. Synthesis and characterization of mesoporous V–Mo-MCM-41 nanocatalysts: Enhancing efficiency in oxalic acid synthesis. *Heliyon* **2024**, *10*, 24652. Doi: 10.1016/j.heliyon.2024.e24652
34. Thu, J.; Dutta, P.K.; Kresge, C.T. Raman spectroscopic studies of the synthesis of faujasitic zeolites: Comparison of two silica sources. *Zeolites* **1991**, *11*, 672-679. Doi: 10.1016/S0144-2449(05)80170-8
35. Jin, S.; Feng, Z.; Fan, F.; Li, C. UV Raman Spectroscopic Characterization of Catalysts and Catalytic Active Sites. *Catal Lett* **2015**, *145*, 468–481. Doi: 10.1007/s10562-014-1416-0
36. Lewandowska, A.E.; Banares, M.A.; Tielens, F.; Che, M.; Dzwigaj, S. Different Kinds of Tetrahedral V Species in Vanadium-Containing Zeolites Evidenced by Diffuse Reflectance UV-vis, Raman, and Periodic Density Functional Theory. *J. Phys. Chem. C* **2010**, 114, 19771–19776. Doi: 10.1021/jp107589d
37. Zhang, Q.; Wang, Y.; Ohishi, Y.; Shishido, T.; Takehira, K. Vanadium-Containing MCM-41 for Partial Oxidation of Lower Alkanes. *J. Catal*. **2002**, 202, 308–318. Doi: 10.1006/jcat.2001.3276
38. Wetherall, K.M.; Doughty, P.; Mountjoy, G.; Bettinelli, M.; Speghini, A.; Casula, M.F.; Cesare-Marincola, F.; Locci, E.; Newport, R. J. The atomic structure of niobium and tantalum containing borophosphate glasses. *J. Phys.: Condens. Matter* **2009**, *21*, 375106. Doi: 10.1088/0953-8984/21/37/375106
39. Aspromonte, S.G.; Sastre, Á.; Boix, A.V.; Cocero, M.J.; Alonso, E. Cobalt oxide nanoparticles on mesoporous MCM-41 and Al-MCM-41 by supercritical CO_2 deposition. *Micropor. Mesopor. Mater.* **2012**, *148*, 53-61. Doi: 10.1016/j.micromeso.2011.07.014
40. Yu, J.; Feng, Z.; Xu, L.; Li, M.; Xin, Q.; Liu, Z.; Li, C. Ti-MCM-41 Synthesized from Colloidal Silica and Titanium Trichloride: Synthesis, Characterization, and Catalysis. *Chem. Mater.* **2001**, *13*, 994-998. Doi: 10.1021/cm000758h
41. Nitsche, D.; Hess, C. Structure of Isolated Vanadia and Titania: A Deep UV Raman, UV−Vis, and IR Spectroscopic Study. *J. Phys. Chem. C* **2016**, *120*, 1025−1037. Doi: 10.1021/acs.jpcc.5b10317
42. Malfait, B.; Moréac, A.; Jani, A.; Lefort, R.; Huber, P.; Fröba, M.; Morineau, D. Structure of Water at Hydrophilic and Hydrophobic Interfaces: Raman Spectroscopy of Water Confined in Periodic Mesoporous (Organo)Silicas. *J. Phys. Chem.* C, **2022**, 126, 3520-3531. Doi: 10.1021/acs.jpcc.1c09801
43. Kondratenko, E.V.; Cherian, M.; Baerns, M.; Su, D.; Schlögl, R.; Wang, X.; Wachs, I.E. Oxidative dehydrogenation of propane over V/MCM-41 catalysts: comparison of O_2 and N_2O as oxidants. *J. Catal.* **2005**, 234, 131–142. Doi: 10.1016/j.jcat.2005.05.025
44. Petrescu, S.; Constantinescu, M.; Anghel, E.M.; Atkinson, I.; Olteanu, M.; Zaharescu, M. 52. Structural and physico-chemical characterization of some soda lime zinc alumino-silicate glasses. *J Non-Crystall Solids* **2022**, 358, 3280-3288. Doi: 10.1016/j.jnoncrysol.2012.09.00100
45. Lee, E.L.; Wachs, I.E. In Situ Spectroscopic Investigation of the Molecular and Electronic Structures of SiO_2 Supported Surface Metal Oxides, *J. Phys. Chem. C* **2007**, *111*, 14410-14425. Doi: 10.1021/jp0735482
46. Liu, W.-S.; Liao, M.-W.; Huang, S.-H.; Reyes, Y. L. A.; Chen, H.-Y.T.; T.-P. Perng, T.-P. Formation and characterization of gray Ta_2O_5 and its enhanced photocatalytic hydrogen generation activity. *Int. J. Hydr Energ* **2020,** *45*, 16560-16568. Doi: 10.1016/j.ijhydene.2020.04.154
47. Xiong, G.; Li, C.; Li, H.; Xin, Q.; Feng, Z. Direct spectroscopic evidence for vanadium species in V-MCM-41 molecular sieve characterized by UV resonance Raman spectroscopy. *Chem. Commun*., **2000**, 677–678. Doi: 10.1039/b000557f
48. Gao, X.; Wachs, I.E.; Wong, M.S.; Ying, J.Y. Structural and Reactivity Properties of Nb–MCM-41: Comparison with That of Highly Dispersed Nb_2O_5/SiO_2 Catalysts. *J. Catal.* 2001, *203*, 18–24. Doi:10.1006/jcat.2001.3313
49. Suib, S. L.; Přech, J.; Szaniawska, E.; Čejka, J. Recent Advances in Tetra- (Ti, Sn, Zr, Hf) and Pentavalent (Nb, V, Ta) Metal-Substituted Molecular Sieve Catalysis. *Chem. Rev.* **2023**, *123*, 877−917. Doi: 10.1021/acs.chemrev.2c00509
50. Wachs, I.E.; Chen,Y.; Jehng,J.-M.; Briand, L.E.; Tanaka, T. Molecular structure and reactivity of the Group V metal oxides. *Catal. Today* **2003**, 78, 13–24. Doi: 10.1016/S0920-5861(02)00337-1
51. Pedersen, C.S.; Chang, J.H.; Li, Y.; Pryds, N.; Garcia Lastra, J. M. Phase separation in amorphous tantalum oxide from first principles. *APL Mater.* **2020**, 8, 071108. https://doi.org/10.1063/5.0011390
52. Qiyang Lu, G. How to Correctly Analyze 2p X-ray Photoelectron Spectra of 3d Transition-Metal Oxides: Pitfalls and Principles, *ACS Nano* **2024**, 18, 13973−13982. https://doi.org/10.1021/acsnano.4c03964

53. Prokopenko, V.B.; Gurin, V.S.; Alexeenko, A.A.; Kulikauskas, V.S.; D L Kovalenko, D.I. Surface segregation of transition metals in sol–gel silica films. *J. Phys. D: Appl. Phys*. **2000**, 33, 3152–3155. Doi: 10.1088/0022-3727/33/24/304
54. Jiangfeng, L.; Xiaoling, L.; Junying, L.; Ximing P., Wang, J.; Huang, Z.; Yin, G.; Effects of incorporated vanadium and its chemical states on morphology and mesostructure of mesoporous bioactive glass particles. Microp. Mesop. Mater. **2021,** 319, 111061. Doi: 10.1016/j.micromeso.2021.111061
55. Chen, J.Y.; Leng, Y.X.; Zhang, X.; Yang, P.; Sun, H.; Wang, J.; Wan, G.J.; Zhao, A.S.; Huang, N.; Chu, P.K. Effect of tantalum content of titanium oxide film fabricated by magnetron sputtering on the behavior of cultured human umbilical vein endothelial cells (HUVEC). *Nucl. Instrum. Methods Phys. Res.* B **2006**, 242, 26–29. Doi: 10.1016/j.nimb.2005.08.098
56. Martinez, M.; Chourasia, A.R. Characterization of Ti/SnO_2 Interface by X-ray Photoelectron, Spectroscopy. Nanomater. **2022**, 12, 202. Doi: 10.3390/nano12020202
57. Suib, S. L.; Prěch, J.; Szaniawska, E.; Čejka, J. Recent Advances in Tetra- (Ti, Sn, Zr, Hf) and Pentavalent (Nb, V, Ta) Metal-Substituted Molecular Sieve Catalysis, *Chem. Rev.* **2023**, 123, 877−917. Doi: 10.1021/acs.chemrev.2c00509
58. Dupin, J.-C.; Danielle Gonbeau,D.; Vinatier, P.; Levasseur, A. Systematic XPS studies of metal oxides, hydroxides and peroxides. *Phys. Chem. Chem. Phys.* **2000**, 2, 1319-1324. Doi: 10.1039/a908800h
59. Chao, K. J.; Wu, C. N.; Chang, H. Incorporation of Vanadium in Mesoporous MCM-41 and Microporous AFI Zeolites. *J. Phys. Chem. B* **1997,** 101, 6341-6349. Doi: 10.1021/jp970609v
60. Galacho, C.; Ribeiro Carrott, M.; Carrott, Peter; Cansado, I. Hydrothermal Stability of Ordered Mesoporous Titanosilicate Materials Prepared at Room Temperature. *Adv. Mater. Research* **2010,** 107, 63-70. Doi: 10.4028/www.scientific.net/AMR.107.63
61. Garcia, L. M. P.;Tavares, M. T. S.; Andrade Neto, N. F.; Nascimento, R. M.; · Paskocimas, C. A.; ·Longo, E.; Bomio, M. R. D.; Motta, F. V. Photocatalytic activity and photoluminescence properties of TiO_2, In_2O_3,TiO_2/In_2O_3 thin films multilayer. *J. Mater. Sci: Mater Electron* **2018**, 29, 6530–6542. Doi: 10.1007/s10854-018-8635-x
62. Chen, Y.; Zhou, X.; Zha, X.; He, X.; Gu, X. Crystallite structure, surface morphology and optical properties of In_2O_3– TiO_2 composite thin films by sol–gel method. Mater. Sci. Eng. B. **2008,** 151, 179–186. Doi: 10.1016/j.mseb.2008.05.019
63. Liu, Y.; Xu, L.; Xin, Y.; Liu, F.; Xuan, J.; Guo, M.; Duan, T. IrO_2-Ta_2O_5 Anode for Oxygen Evolution with TaOx Interlayer Prepared by Thermal Decomposition in Inert Atmosphere. *J. Electrochem. Soc*. **2022**, 169, 046516. Doi: 10.1149/1945-7111/ac65bd
64. Thornburg, N.E.; Thompson, A.B.; Notestein J.M.; Periodic Trends in Highly Dispersed Groups IV and V Supported Metal Oxide Catalysts for Alkene Epoxidation with H_2O_2. *ACS Catal.* **2015**, 5, 5077−5088. Doi: 10.1021/acscatal.5b01105
65. Parvulescu, V.I; Visinescu, C.; Parvulescu, V.; Marcu, V.; Levy, F. Comparative photocatalytic behavior of Ta catalysts prepared by d.c.-sputtering, sol–gel and grafting in acetone degradation. *Catal. Today* **2006**, 118, 433–439. Doi: 10.1016/j.cattod.2006.07.035
66. Hassan, N.S.; Jalil, A.A.; Hitam, C.N.C.; Sawal, M.H.; Rahim, M.N.S.; Hussain, I.; Jusoh, N.W.C.; Saravanan, R.; Prasetyoko, D. Enhanced photooxidative desulphurization of dibenzothiophene over fibrous silica tantalum: Influence of metal-disturbance electronic band structure. *Int. J. Hydrog. Energy* **2023**, 48, 6575-6585. Doi: 10.1016/j.ijhydene.2022.02.008
67. Emeline, A.V.; Zhang, X.; Murakami, T.; Fujishima, A. Activity and selectivity of photocatalysts in photodegradation of phenols. *J. Hazardous Mat*. **2012**, 211– 212, 154– 160. Doi: 10.1016/j.jhazmat.2011.11.078
68. Dionysiou, D. D.; Suidan, M. T.; Baudin, I.; Laıné, J.-M. Effect of hydrogen peroxide on the destruction of organic contaminants-synergism and inhibition in a continuous-mode photocatalytic reactor. *Appl.Catal. B: Environ* **2004,** 50, 259–269. Doi: 10.1016/j.apcatb.2004.01.022
69. Cheng, Y.; Cao, T.; Xiao, Z.; Zhu, H.; Yu, M. Photocatalytic Treatment of Methyl Orange Dye Wastewater by Porous Floating Ceramsite Loaded with Cuprous Oxide. *Coatings* **2022**, 12, 286. Doi: 10.3390/coatings12020286
70. Din, S.T.U.; Xie, W.-F.; Yang, W. Synthesis of Co_3O_4 Nanoparticles-Decorated $Bi_{12}O_{17}Cl_2$ Hierarchical Microspheres for Enhanced Photocatalytic Degradation of RhB and BPA. *Int. J. Mol. Sci.* **2022**, 23, 15028. Doi: 10.3390/ijms232315028
71. Petcu, G.; Anghel, E.M.; Atkinson, I.; Culita, D.C.; Apostol, N.G.; Kuncser, A.; Papa, F.; Baran, A.; Blin, J.-L.; Parvulescu, V. Composite Photocatalysts with Fe, Co, and Ni Oxides on Supports with Tetracoordinated Ti Embedded into Aluminosilicate Gel during Zeolite Y Synthesis. *Gels* **2024**, 10, 129. Doi: 10.3390/gels10020129
72. Makota, O.; Dutková, E.; Briancin, J.; Bednarcik, J.; Lisnichuk, M.; Yevchuk, I.; Melnyk, I. Advanced Photodegradation of Azo Dye Methyl Orange Using H_2O_2-Activated Fe_3O_4@SiO_2@ZnO Composite under UV Treatment. Molecules **2024**, 29, 1190. Doi: 10.3390/molecules29061190

 doi:10.20944/preprints202409.1452.v